

Effects of Non-Photosynthetic Vegetation on Dust Emissions

Xinyue Huang¹ and Hosein Foroutan¹

¹Virginia Tech

November 23, 2022

Abstract

Mineral dust is among the top contributors to global aerosol loads and is an active element in the Earth system. Ability of non-photosynthetic vegetation (NPV) to suppress dust emission has been supported by observations and small-scale studies, but current regional to global scale models fail to include NPV in the vegetation coverage input. In this study, we implemented a satellite-based total vegetation dataset, which included NPV, into a regional atmospheric chemistry model and conducted simulations of the entire year 2016 for the conterminous United States. We also conducted a control simulation using only the photosynthetic vegetation (PV) to analyze the effects of NPV on dust emissions. Above 10% decreases in simulated dust emissions are seen over most of the southwestern United States from spring to autumn due to NPV. Reductions in dust concentrations are the largest in spring, and when compared to observations, attenuate the overpredictions of fine soil concentrations at over 93% of the observation sites in the western U.S. Further analyses of essential parameters to the inclusion of NPV indicate that sheltering the surface and increasing the threshold velocity through drag partitioning are major mechanisms for the suppression of dust emissions. On the other hand, NPV causes the friction velocity to increase by more than 10% over most erodible lands during autumn and winter, which can amplify the dust flux. This study highlights the necessity of including NPV into the dust model and states that uncertainty analyses of total vegetation datasets are important.

Effects of Non-Photosynthetic Vegetation on Dust Emissions

Xinyue Huang¹ and Hosein Foroutan¹

¹Department of Civil and Environmental Engineering, Virginia Tech, Blacksburg, Virginia, USA

Corresponding author: Hosein Foroutan (hosein@vt.edu)

Key Points:

- A satellite-based total vegetation dataset is implemented in a dust emission model
- Non-photosynthetic vegetation (NPV) reduces dust concentrations by over 10% in most areas of the southwestern U.S. from spring to autumn
- NPV suppresses dust emissions mainly by sheltering the ground surface and raising the threshold velocity

11 **Abstract**

12 Mineral dust is among the top contributors to global aerosol loads and is an active element in the
13 Earth system. Ability of non-photosynthetic vegetation (NPV) to suppress dust emission has
14 been supported by observations and small-scale studies, but current regional to global scale
15 models fail to include NPV in the vegetation coverage input. In this study, we implemented a
16 satellite-based total vegetation data, which included NPV, into a regional atmospheric chemistry
17 model and conducted simulations of the entire year 2016 for the conterminous United States. We
18 also conducted a control simulation using only the photosynthetic vegetation (PV) to analyze the
19 effects of NPV on dust emissions. Above 10% decreases in simulated dust emissions are seen
20 over most of the southwestern United States from spring to autumn due to NPV. Reductions in
21 dust concentrations are the largest in spring, and when compared to observations, attenuate the
22 overpredictions of fine soil concentrations at over 93% of the observation sites in the western
23 U.S. Further analyses of essential parameters to the inclusion of NPV indicate that sheltering the
24 surface and increasing the threshold velocity through drag partitioning are major mechanisms for
25 the suppression of dust emissions. On the other hand, NPV causes the friction velocity to
26 increase by more than 10% over most erodible lands during autumn and winter, which can
27 amplify the dust flux. This study highlights the necessity of including NPV into the dust model
28 and states that uncertainty analyses of total vegetation datasets are important.

29 **Plain Language Summary**

30 Severe dust-emission events can interrupt traffic, damage infrastructure, and incur cleaning
31 expenses locally. Dust particles that are lifted into the air by wind are also associated with global
32 health problems and climate effects. Most of the global dust emissions come from arid or semi-
33 arid environments where the brown vegetation is abundant, and the amount of dust emissions is
34 thus modulated by the presence of brown vegetation. However, current atmospheric models omit
35 brown vegetation because it cannot be detected easily similar to green vegetation. In this study,
36 we provided a total vegetation (sum of green and brown vegetation) dataset as an input to an
37 atmospheric chemistry model, and simulated annual dust emissions over the conterminous
38 United States. We find that the brown vegetation reduces the dust concentrations in air by above
39 10% over most of the southwestern U.S. from spring to autumn. The reductions are mainly
40 because the brown vegetation directly protects the surface from wind erosion, as well as reduces
41 the drag on the surface such that a minimum wind speed needed to initiate dust emissions
42 becomes higher.

43 **1. Introduction**

44 Mineral dust aerosols emitted by wind erosion play an active role in affecting human
45 health and activities (Baddock et al., 2014; Nakao et al., 2018; Al-Hemoud et al., 2019),
46 impacting the climate (Miller, 1998; Schepanski, 2018), and transporting nutrients and
47 microorganisms (Csavina et al., 2012; Kellogg & Griffin, 2006). The global emissions of dust
48 particles are mainly from arid or semi-arid environments (Knippertz, 2017) and are modulated by
49 non-photosynthetic vegetation (NPV), which is predominant in these regions (Jacques et
50 al., 2014). NPV includes dead leaves, crop residuals, and litters (Guerschman et al., 2009; Ji et
51 al., 2020). Negative relations between the amount of dead leaves on the ground and the
52 frequency of dust outbreaks are supported by interannual observations (Kurosaki et al., 2011;
53 Nandintsetseg & Shinoda, 2015). Also, the relations between soil erosion and the coverage of

54 flat and standing crop residues were quantified, and the underlying mechanisms were studied on
55 small scale uniform or experimental fields (Hagen, 1996; Lin et al., 2021).

56 The challenge to extend this knowledge to regional-to-global scales lays in providing
57 accurate information about the temporally and spatially variant vegetation to atmospheric
58 models. In practice, the parameterization of vegetation in windblown dust schemes implemented
59 in current chemical transport models or general circulation models relies on data for vegetation
60 fractional coverage (Duncan Fairlie et al., 2007; Foroutan et al., 2017; LeGrand et al., 2019;
61 Zhang et al., 2012). However, the vegetation fractional maps used by these models are often
62 based on readily available vegetation indices from satellite retrievals which only represents
63 photosynthetic vegetation (PV) (e.g., fraction of absorbed photosynthetically active radiation
64 (FPAR) or normalized difference vegetation index (NDVI)).

65 To the authors' knowledge, there has been only one attempt to address this failure of
66 accounting for NPV in the vegetation map used to simulate regional dust emissions (Kang et al.,
67 2014). The researchers estimated the NPV fractions in East Asia by assuming that the NPV
68 fractions follow a linear decrease from the maximum fractions of green vegetation from last
69 year. The conclusion that the approximated NPV fractions improved the simulation for a dust
70 event can be further validated with a more realistic representation of NPV coverage that accounts
71 for the non-linear growth-decay cycle of plants in different environments. The total vegetation
72 (sum of PV and NPV) data was made available in the Multiscale Online Non-Hydrostatic
73 Atmosphere Chemistry (MONARCH) model version 2.0 model as recently reported (Klose et
74 al., 2021) and more studies on the relations between NPV and dynamics of dust emissions are
75 anticipated.

76 Remote sensing techniques have a high potential to capture the heterogeneity of
77 vegetation compared to field measurements or ecosystem modeling at a larger scale (Mougin et
78 al., 1995). These techniques can identify NPV elements based on their different reflectance
79 spectrum in the visible light to short-wave infrared regions, due to their lower pigments and
80 water contents than PV, and higher cellulose and lignin contents than soils (Z. Li & Guo, 2015).
81 Multispectral imagery is more widely used than hyperspectral imagery at large scales due to
82 availability (Z. Li & Guo, 2015). Several vegetation indices that represent NPV coverage
83 calculated from selected bands of multispectral reflectance have been developed, such as the
84 Normalized Difference Senescent Vegetation Index (NDSVI) (Qi & Wallace, 2002), the Soil
85 Adjusted Total Vegetation Index (SATVI) (Marsett et al., 2006), and the Dead Fuel Index (DFI)
86 (Cao et al., 2010), but they are generally considered to be site-specific (X. Li et al., 2016).
87 Another technique to acquire NPV fractions is the spectral mixture analysis (SMA) which uses
88 all bands of the reflectance spectrum (Asner & Heidebrecht, 2002). The SMA method assumes
89 that the surface reflectance is a combination of the reference reflectance of certain surface
90 components or endmembers, and then resolves the fractions of all endmembers given their
91 reference spectra. Variations of SMA methods (X. Li et al., 2016; Okin et al., 2013) mostly differ
92 in the selection of reference spectra and comparisons among these variations showed that
93 allowing the spectra for a certain endmember to vary among pixels improved the estimation of
94 fractions.

95 This study is aimed at testing the effects of NPV on the seasonal dust emissions, and
96 understanding the underlying mechanisms. We implemented satellite-based maps for both PV
97 and NPV fractions derived using a SMA method into the windblown dust scheme in the
98 Community Multiscale Air Quality (CMAQ) model and conducted simulations for the entire

99 year 2016 over the conterminous United States (CONUS) (hereafter the TOTAL run). We also
100 conducted a control run with PV only coverage data represented by the FPAR from the Moderate
101 Resolution Imaging Spectroradiometer (MODIS) instrument (hereafter the FPAR run) and then
102 contrasted the results. Section 2 describes the methods for generating the vegetation data, the
103 parameterization of vegetation in our dust model, and the evaluation methodology. The results
104 are presented and discussed in Section 3. Finally, summaries of our major findings, discussion of
105 uncertainties, and future improvements are included in Section 4.

106 **2. Methods**

107 2.1. Vegetation Data

108 In this study, we used two datasets for vegetation fractional coverage. The total
109 vegetation data was obtained from the MODIS Nadir BRDF-Adjusted Reflectance (MCD43A4)
110 product collection 5, which has a spatial and temporal resolution of 500 m and every 16 days,
111 respectively. Details about the spectral unmixing analysis (SMA) method used to develop this
112 dataset have been described in Guerschman et al. (2015) and Scarth et al. (2011). In brief, a
113 linear unmixing method was performed to calculate the fractions of three pure surface
114 components, namely PV, NPV, and bare soils based on the observed surface reflectance and the
115 synthetic reference reflectance of the three components. Synthetic reference reflectance was
116 derived from field measurements of vegetation fractional cover and satellite imagery using a
117 multiple regression model. Seven bands of the reflectance from the MCD43A4 product were
118 used to perform the unmixing, as well as their log transforms and interactive terms to account for
119 the non-linear spectral mixing. To avoid overfitting, a subspace truncation method was applied to
120 control the number of reflectance terms used for unmixing and that number was determined with
121 a 100-fold cross-validation method. During the unmixing, the three fractions in each pixel were
122 constrained to be non-negative and must add up to 100%. The resulting dataset includes monthly
123 averaged vegetation fractions at 5 km resolution. It was re-gridded to 12 km over the study
124 domain using the nearest-neighbor space-filling method. The processed monthly data was then
125 transformed into daily data using linear interpolation, and meanwhile, some missing values were
126 replaced using values from consecutive months. For a small amount of grid cells with missing
127 values throughout the year, the total vegetation fractions were set to be 1. The rationale was that
128 the missing values were likely due to snow cover because most of those grids were in the north
129 of the study domain, and a complete coverage of vegetation would eliminate the dust emissions
130 from these cells just as snow cover. Details about this dataset are discussed in Section 3.1.

131 The other dataset uses an index for green vegetation, the fraction of photosynthetic active
132 radiation (FPAR). The FPAR data was retrieved from the MODIS15A2GFS satellite product
133 with 1 km resolution and every 8 days and then re-gridded and interpolated to a daily 12 km-
134 resolution dataset. This approach and the resulting dataset have been previously used in WRF-
135 CMAQ simulations by Ran et al. (2016) and Foroutan and Pleim (2017).

136 2.2. Parameterization of Vegetation in the Dust Model

137 The windblown dust scheme used in CMAQ is a physics-based model described in
138 details by Foroutan et al. (2017). Here, we present a short overview of the scheme and focus on
139 the representation of vegetation in the model. Saltation bombardment is deemed as the main

140 mechanism of aeolian dust emissions. The module calculates the bulk dust emission and assigns
 141 the total mass into fine and coarse modes. The total mass of vertical dust flux is determined
 142 based on a horizontal flux and a vertical-to-horizontal flux ratio. The latter is dependent on soil
 143 properties and scales with the friction velocity (Lu & Shao, 1999). The total horizontal dust flux
 144 is calculated by integrating the horizontal fluxes of particles in each size bin:

$$145 \quad F_H(D) = \begin{cases} C \frac{\rho_a}{g} u_*^3 \left(1 - \frac{u_{*,t}(D)}{u_*}\right) \left(1 + \frac{u_{*,t}(D)}{u_*}\right)^2, & u_{*,t} < u_* \\ 0, & u_{*,t} \geq u_* \end{cases} \quad (1)$$

146 where C is a constant of proportionality set to 1.0, ρ_a is the air density, and $u_{*,t}$ is the threshold
 147 friction velocity.

148 The threshold friction velocity governs the initiation of saltation. It is modeled as an ideal
 149 threshold friction velocity corrected with two factors for soil moisture and roughness elements.

$$150 \quad u_{*,t} = u_{*,t0} f_m f_r \quad (2)$$

151 Here, $u_{*,t0}$ is the ideal threshold velocity for dry and smooth surfaces. The f_m and f_r are
 152 correction factors for soil moisture and surface roughness, respectively, both of which are equal
 153 or greater than 1.0. The soil moisture factor is determined according to a model by F. FeÂcan
 154 (1999). The roughness factor is determined using a double drag partitioning concept to take both
 155 the solid elements and the vegetation into account (Darmenova et al., 2009; Raupach et al.,
 156 1993).

$$157 \quad f_r = (1 - \sigma_v m_v \lambda_v)^{0.5} (1 + \beta_v m_v \lambda_v)^{0.5} \left(1 - \sigma_s m_s \frac{\lambda_s}{1 - A_v}\right)^{0.5} \left(1 + \beta_s m_s \frac{\lambda_s}{1 - A_v}\right)^{0.5} \quad (3)$$

158 Here, σ_v and σ_s are the basal-to-frontal area ratios of vegetation and solid elements, β_v and β_s
 159 are ratios of drag coefficients on vegetation and solid elements to the drag coefficient on bare
 160 surface, m_v and m_s account for the differences between average surface stress and maximum
 161 surface stress, A_v is the fractional coverage of total vegetation, and λ_v and λ_s are surface
 162 roughness density of vegetation and solid elements. We used the same values as Darmenova et

163 al. (2009) for σ_v , σ_s , β_v , β_s , m_v , and m_s . Values for λ_s for each landuse type were adapted from
 164 Xi and Sokolik (2015) and Darmenova et al. (2009).

165 The λ_v is calculated from vegetation coverage, A_v following a relation proposed by Shao
 166 et al. (1996).

$$167 \quad \lambda_v = -0.35 \ln(1 - A_v) \quad (4)$$

168 According to Foroutan et al. (2017), the surface wind friction velocity should be
 169 corrected for dust emissions calculations:

$$170 \quad u_* = \kappa U_{10} \ln\left(\frac{z_0}{10}\right) \quad (5)$$

171 where κ is the von Kármán constant, U_{10} is the 10-m wind speed, and z_0 is the surface roughness
 172 length relevant to dust emission processes.

173 The z_0 scales with the physical height of roughness elements on the surface. To determine
 174 z_0 , we adapted the empirical relation developed by Foroutan et al. (2017).

$$175 \quad z_0/h = \begin{cases} 0.96\lambda^{1.07}, & \lambda < 0.2 \\ 0.083\lambda^{-0.46}, & \lambda \geq 0.2 \end{cases} \quad (6)$$

176 where λ is the total roughness density, and it is defined as the sum of roughness density for solid
 177 elements and total vegetation ($\lambda = \lambda_s + \lambda_v$). The h is the total effective height of roughness
 178 elements. In this study, the effective heights of roughness components were updated with the
 179 inclusion of NPV. It was calculated as the weighted average of roughness heights based on
 180 roughness density:

$$181 \quad h = \frac{h_{PV}\lambda_{PV} + h_{NPV}\lambda_{NPV} + h_s\lambda_s}{\lambda_{PV} + \lambda_{NPV} + \lambda_s} \quad (7)$$

182 The set of vegetation heights in Foroutan et al. (2017) basically represents the growth-
 183 decay cycle of green vegetation and they were preserved to serve as the height for PV (h_{PV}) in
 184 this study (Table 1). Since the phenological and geometric characteristics of dead plant and litter
 185 are different from that of PV, a look-up table for the NPV heights were predefined and added to
 186 the model. The assignment of the NPV heights considered the seasonal variation, which was
 187 implied from the trends of biomass observed in field measurements and modeling practices
 188 (Nandintsetseg & Shinoda, 2015; Pierre et al., 2015). The NPV heights reaches their peak in
 189 September or October, which is consistent with the evidence that the biomass of senescent plants
 190 in grassland peaked between September and November and that the interannual averaged
 191 senescence period for typical steppe plants was between September and October (Shinoda et al.,
 192 2011). Considering the biomass of NPV did not exceed the biomass of PV, the maximum heights

193 for NPV were set to be lower than the maximum PV heights. These features were captured in the
 194 assigned heights for NPV as shown in Table 1.

195

196 **Table 1.** Predefined Heights for PV and NPV. All units are in cm.

		Jan	Feb	Mar	Apr	May	Jun	Jul	Aug	Sep	Oct	Nov	Dec
Shrubland	PV	5	5	15	15	12	12	10	10	10	5	5	5
	NPV	6	6	5	5	5	5	5	5	6	8	8	6
Grass	PV	5	5	5	10	20	15	12	12	10	5	5	5
	NPV	8	5	5	5	5	5	5	5	10	10	8	8
Barren	PV	5	5	10	10	10	10	10	10	10	10	5	5
	NPV	4	4	4	3	3	3	3	3	5	5	5	5
Crop	PV	5	5	5	5	10	30	50	50	30	10	5	5
	NPV	8	8	5	5	5	5	5	5	15	15	10	10

197

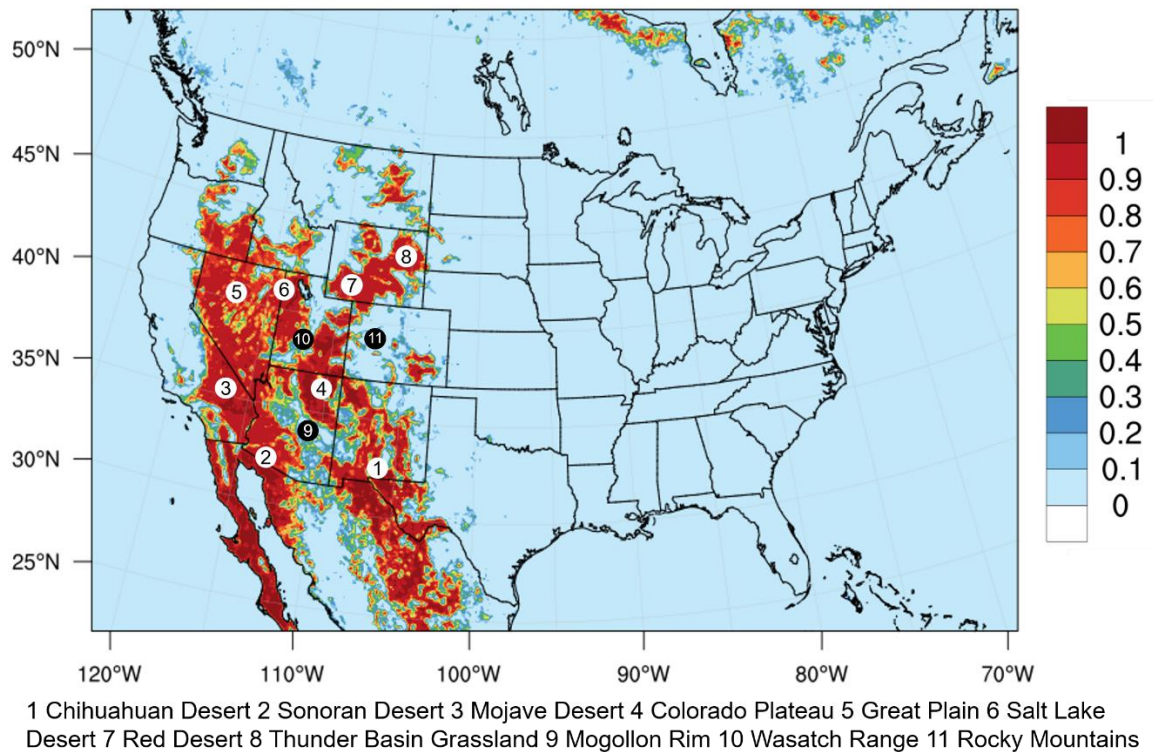
198 In general, it can be seen that the vegetation coverage is as an important component of
 199 the dust scheme which not only determines the fractions of available surface to wind erosion, but
 200 also alters the friction velocity u^* (via surface roughness length, Eq. (6)) and its threshold value
 201 u^*_{t} (via surface roughness factor, Eq. (3)).

202 2.3. Model Setup

203 The CMAQ model version 5.3 (Appel et al., 2020) was used in this study. The model
 204 domain consisting of the CONUS, as well as parts of Mexico and Canada (Figure 1) was
 205 discretized using a 12-km horizontal grid and 35 vertical layers. Simulations were performed for
 206 the entire year 2016 with a clean initial condition and 10-day spin-up time. The meteorological
 207 inputs to CMAQ were generated by a Weather Research and Forecasting (WRF) model version
 208 3.8 simulation and then processed with the Meteorology-Chemistry Interface Processor (MCIP)
 209 version 5.0. Anthropogenic emissions input data was provided by the emissions modeling
 210 platform run by US EPA and biogenic emissions were calculated in-line. The boundary
 211 conditions were derived from hemispheric simulations of CMAQv53. The Biogenic Emission
 212 Landcover Database version 3 (BELD3) was used in the dust scheme and three land use types
 213 were considered as erodible land, namely USGS_shrubland, USGS_shrubgrass, and
 214 USGS_sprsbaren. The total fractions of these three types of erodible lands are shown in Figure
 215 1. The soil type information was based on US State Soil Geographic (STATSGO) soil database
 216 (R. L. Miller, 1998) and four soil textures (clay, silt, fine-to-medium sand, and coarse sand) were
 217 identified for each soil type following Tegen et al. (2002). Ammonia bi-directional flux and
 218 updated M3dry model were used for deposition. CB06r3 chemical mechanism and AERO7

219 aerosol model were used for atmospheric chemistry. Details on all other settings as well as the
 220 model evaluation can be found in Appel et al. (2020).

221



222 **Figure 1.** The total fractions of three types of erodible landuse (*USGS_shrubland*,
 223 *USGS_shrubgrass*, and *USGS_sprsbarrren*) based on BELD3, along with annotations for
 224 geographic names used in this paper.
 225

226

227 2.4. Evaluation Methodology

228 The windblown dust emissions in CMAQ are confined to erodible lands, so the
 229 evaluation of dust simulations was focused on the western states. Dust events are essential
 230 sources for minerals in the air. Therefore, we used observed “fine soil” (hereafter simply soil)
 231 concentrations as defined by the Interagency Monitoring of Protected Visual Environments
 232 (IMPROVE) sites (<http://vista.cira.colostate.edu/Improve/>) to evaluate the simulations. The
 233 IMPROVE network was designated to monitor the visibility in national parks and its sites
 234 concentrate in the western United States. The observatory data were available throughout 2016

235 every three days. The outputs from the CMAQ model were post-processed and the soil
 236 concentrations were calculated following the equation for soil adapted by the IMPROVE sites.

$$237 \quad [Soil] = 2.2[Al] + 2.49[Si] + 1.63[Ca] + 2.42[Fe] + 1.94[Ti] \quad (8)$$

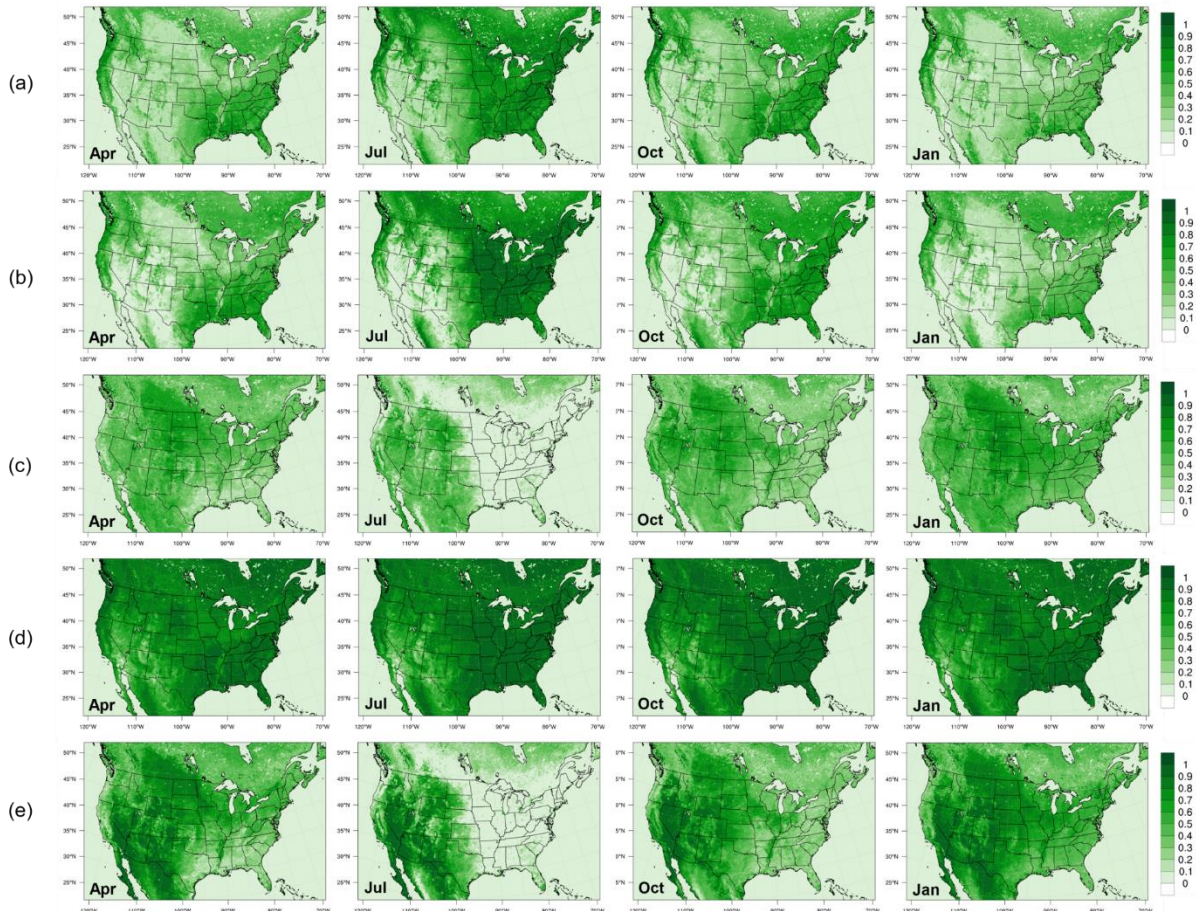
238 This equation considered the chemical composition of the oxides for predominant elements in
 239 soil (Malm, 1994).

240 The mean bias (MB), the normalized mean bias (NMB), the mean error (ME), the
 241 normalized mean error (NME), and the Pearson correlation coefficient between simulations and
 242 observations were used to access the simulated results.

243 3. Results and Discussion

244 3.1. Vegetation Coverage

245

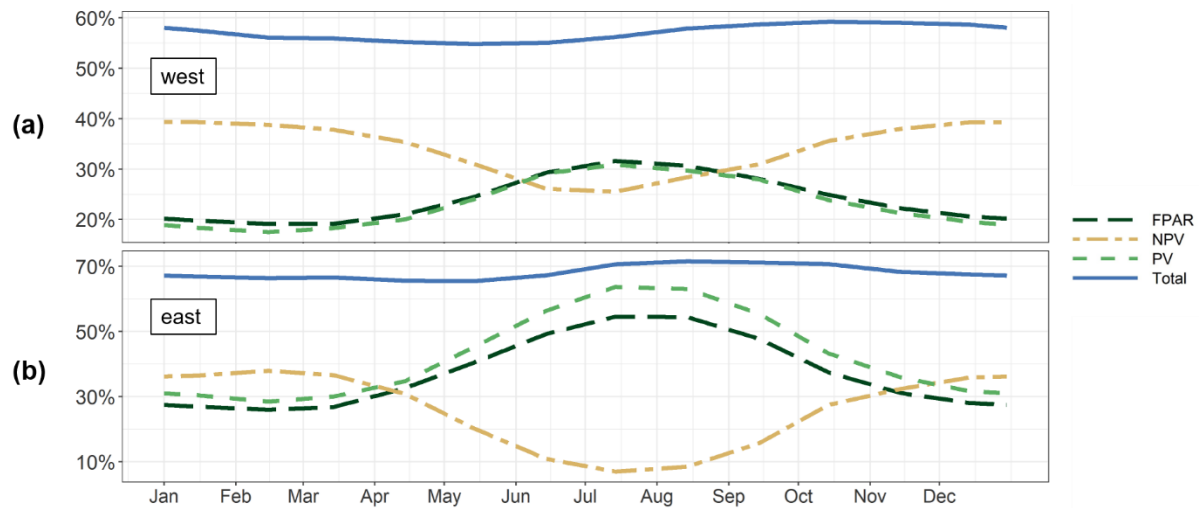


246 **Figure 2.** Spatial distributions of (a) the MODIS FPAR, (b) the PV fractions, (c) the NPV fractions,
 247 (d) the total vegetation fractions derived from MODIS surface reflectance using SMA, and (e) the
 248 ratio of NPV to total vegetation fractions at the 15th of the middle month in each season.
 249

250 We present snapshots of the MODIS FPAR and the fractions of PV, NPV, and total
 251 vegetation obtained following procedures discussed in Sec. 2.1 in the middle of each season, as
 252 well as the ratio of NPV to total vegetation fractions in Figure 2. Clear contrasts between the
 253 eastern and the western parts of the region are seen in maps for green and brown vegetation
 254 (Figure 2(a)-(c)), which are most apparent in summer. The seasonal variation of both green and
 255 brown vegetation is higher in the east than in the west. Therefore, for the purpose of quantitative
 256 analysis, we averaged the vegetation fractions over the east and the west, separately. The
 257 separation was chosen to be along 97°W with consideration of both our vegetation maps and the
 258 shifted 100th meridian. The 100th meridian is a historical divide between the humid eastern and
 259 the arid western America, and it was found to shift eastwards due to climate change and human
 260 activities over past centuries (Seager, Feldman, et al., 2018; Seager, Lis, et al., 2018). The
 261 resulting averaged vegetation fractions from two datasets over the east and the west throughout
 262 2016 are shown in Figure 3.

263

264



265

266 **Figure 3.** Averaged MODIS FPAR, PV, NPV, and total vegetation fractions over (a) the western
 267 and (b) the eastern study domain during 2016.

268

269 The vegetation fractions derived using the same SMA method were evaluated for
 270 Australia, and the RMSE for PV, NPV, and bare soil fractions were 0.13, 0.18, and 0.16,
 271 respectively (Guerschman et al., 2015). But these uncertainties are unknown for the vegetation
 272 data over the North America. To understand the reliability of the total vegetation maps, we
 273 compared the green vegetation coverage from two datasets. The MODIS FPAR (Figure 2(a)) and
 274 the PV fractions derived using the SMA technique (Figure 2(b)) agree well in spatial distribution
 275 across all seasons. Both of the coverages are relatively high in the Rocky Mountains, the
 276 Wasatch Range, and the Mogollon Rim in the western U.S., and they decrease northwestwards
 277 from the southeast coast in the eastern U.S. The averaged MODIS FPAR and SMA derived PV
 278 fractions differ by less than 9% in the east and 2% in the west throughout 2016. The comparable

279 values of PV fractions and MODIS FPAR demonstrate that the SMA method is generally good at
280 resolving green vegetation over the study domain.

281 The NPV coverage in general has reversed spatial and temporal patterns relative to the
282 green vegetation coverage. The percentage of NPV is relatively low in the forested regions in the
283 west, and has a positive gradient in the Midwest. The average NPV fraction ranges between 26%
284 and 40% over the western and between 7% and 36% over the eastern part of the CONUS (Figure
285 3). The average NPV fractions are at the minimum in late-June or mid-July, start to increase in
286 August, and reach a maximum from December to February. These seasonal trends resemble the
287 accumulation and decay of senescent plant materials. Note that, the maximum average coverage
288 of NPV (40%) in 2016 exceeds that of PV (31%) in the west. This suggests that there may be
289 other sources of NPV in the winter in addition to withered green vegetation from the same year,
290 probably perennial dead biomass. This might also suggest some overestimations of NPV
291 coverage using the SMA method. In the southwestern U.S., the averaged NPV fractions are high
292 over most arid or semi-arid areas including the Chihuahuan Desert, the Colorado Plateau, the
293 Great Basin, and the northern Great. The NPV coverage varies around 40%-50% across the year
294 in these areas. In forested areas in the southwest where PV fractions are relatively high, the NPV
295 coverage varies around 30% in 2016.

296 Maps for the ratios of NPV to total vegetation coverage or the relative ratios of NPV
297 (Figure 2(e)) have similar spatial distribution as the NPV fractions, but with stronger contrasts.
298 These maps highlight areas where NPV is the dominant component of vegetation. In the western
299 U.S., the regions with high relative NPV ratio (nearly 100% in winter) greatly overlap with those
300 with the erodible landuse. Most of these areas have high NPV coverage (> 40% in winter), except
301 that the NPV fractions are relatively low (at around 30% in winter) in the Mojave Desert in the
302 southmost corner of California. The relative ratios of NPV are constantly 100% in some
303 southwestern desert lands all year round due to no detection of PV. In forested areas in the
304 southwestern U.S., including the Mogollon Rim and the Rocky Mountains, the relative NPV
305 ratio ranges between 20% and 70%.

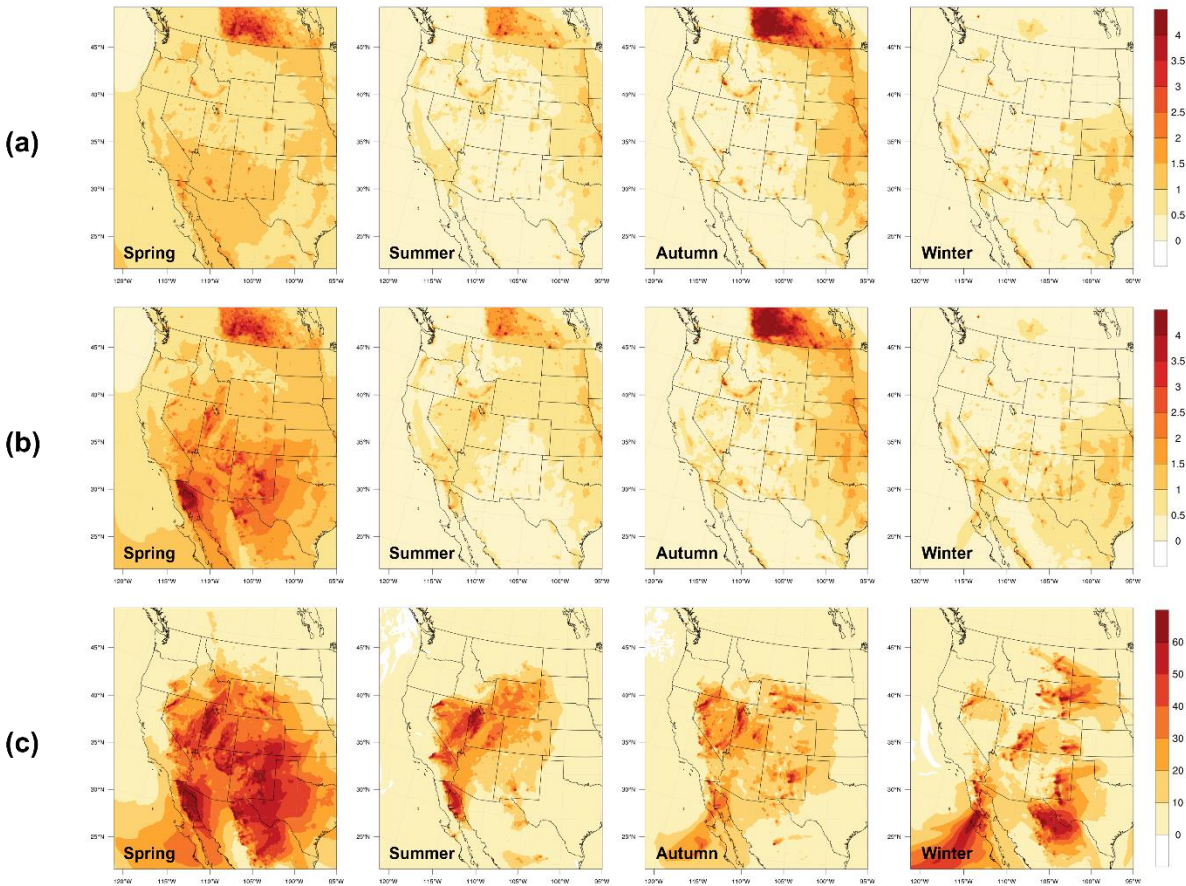
306 The total vegetation coverage seems quite stable over the year (Figure 2(d)), as a result of
307 the opposite spatial and seasonal trend of PV and NPV coverage. The average total vegetation
308 fraction varies slightly around 56% in the west and around 68% in the east over the year. As
309 expected, the coverage is relatively low in desert lands in the southwest. The annual average of
310 total coverage is around 30% in the Great Basin, the Red Desert, the Sonoran Desert, the
311 Colorado Plateau, and the Chihuahuan Desert, and it gradually increases towards the edges of
312 these dry lands, reaching around 60% at the rims.

313 In the west, at places where NPV is abundant (both fractions and relative ratios), the PV
314 is relatively sparse, and the total vegetation coverage is lower than other areas. These NPV-rich

315 regions highly overlap with regions with erodible landuse (see Figure 1). Therefore, NPV is
 316 expected to have an impact on dust emissions from these source regions.

317 3.2 Seasonal Analysis of Dust Emissions

318



319
 320 **Figure 4.** Seasonal averages of modeled soil concentrations ($\mu\text{g}/\text{m}^3$) over the western U.S. from
 321 (a) the TOTAL run and (b) the FPAR run. Row (c) presents the changes in soil concentrations (%)
 322 as percentage of soil concentrations from the FPAR run after replacing the MODIS FPAR data
 323 with the total vegetation data.

324

325 We presented the seasonal averages of simulated soil concentrations from the TOTAL
 326 run and the FPAR run in Figure 4(a) and (b), respectively. Comparisons among all seasons
 327 reveal that spring has the highest soil concentration for both cases. In spring, simulations from
 328 the TOTAL run show that the average soil concentrations are higher (above $1.5 \mu\text{g}/\text{m}^3$) in the
 329 south, including most areas in Arizona and New Mexico, southern California, and northern
 330 Mexico, than other areas. As for the FPAR simulations, soil concentrations are consistently
 331 above $1.5 \mu\text{g}/\text{m}^3$ over the southwestern U.S. during spring and the most pronounced soil
 332 concentrations (above $3 \mu\text{g}/\text{m}^3$) are seen in several sub-regions with desert lands, including the
 333 Salt Lake Desert, the Colorado Plateau, the Sonoran Desert, and the Chihuahuan Desert. The

334 magnitude and spatial distribution of soil concentrations are comparable during summer and
335 autumn for both cases, but more soils are emitted from the Great Basin in summer than in
336 autumn in the FPAR run. The soil emissions in winter are similar to that in autumn, but less in
337 northern states, probably due to snow cover. In general, simulations from both runs are able to
338 capture the seasonal variation of dust emissions and highlight locations with high dust emissions.

339 Then, we analyzed the differences in simulated soil concentrations between the two runs
340 to understand how NPV modulates windblown dust emissions. Figure 4(c) shows the changes in
341 soil concentrations as percentage of the simulations from the FPAR run. Spring witnesses the
342 most dramatic percentage of changes in soil concentrations in terms of affected areas. With the
343 total vegetation data, the seasonal averaged soil concentrations reduce the most (above 50%) in
344 dust source regions that generate the most soils in the FPAR run (Figure 4(b)) as mentioned
345 above. The transport of emitted dust aerosols results in above 30% of changes in soil
346 concentrations over most areas in the southwestern U.S. During summer, averaged soil
347 concentrations reduce by over 50% in the Sonoran Desert and the Salt Lake Desert, and by over
348 20% also in the Mojave Desert, the Great Basin in Nevada, Wyoming, and western Colorado
349 when using the total vegetation data. Changes in soil concentrations during autumn are less
350 significant and over 50% of changes mainly occur over small areas in the Salt Lake Desert,
351 northwestern Nevada, Wyoming, and eastern New Mexico. In winter, soil emissions are most
352 suppressed by NPV in the same dust source regions as those for spring except for the Salt Lake
353 Desert, and in eastern Montana additionally. The reductions in soil emissions by NPV,
354 nevertheless, influence smaller areas downwind. Areas include the southern Nevada, western
355 Utah, eastern Arizona, and western New Mexico experience less than 10% of change in soil
356 concentrations, likely due to the relatively short-range transport of dust plumes.

357 Most areas in the southwestern U.S. experience above 10% of reductions in soil
358 concentrations after replacing the MODIS FPAR data with the total vegetation data during all
359 seasons but winter. Highest percentage (above 50%) of changes in soil concentrations are seen in
360 dust source regions with high NPV fractions ($> 40\%$ in winter). Regions with large percentage of
361 differences across multiple seasons highlight places where the dust emissions are most
362 susceptible to NPV. These regions include the Sonoran Desert in Baja California, Mexico, the
363 Chihuahuan Desert in New Mexico, the Great Basin in northwestern Nevada, and the Colorado
364 Plateau in southeastern Utah, where the seasonal averaged soil concentrations are significantly
365 suppressed by NPV throughout the year. Besides, the reductions in soil emissions induced by
366 NPV are significant in the Salt Lake Desert throughout the year except in winter.

367 To shed light on the performances of the two model runs, we evaluated the simulations of
368 soil concentrations from both runs with ground observations from the IMPROVE sites. The
369 statistics of the models' performances over selected western states during each season are
370 presented in Table 2. Selected states are Wyoming, Nevada, Utah, Colorado, Arizona, and New
371 Mexico, which cover most of the active dust source regions in the U.S.

372 During spring, the normalized mean bias (NMB) of simulated soil concentrations from
373 the TOTAL run (3.6%) is much smaller than that from the FPAR run (72.8%). The correlation
374 coefficient between simulations and observations also increases from 0.44 to 0.52 when
375 replacing MODIS FPAR with total vegetation. The similar results are seen in winter, when the
376 NMB decreases by more than a half with total vegetation. In general, including NPV into the

377 model attenuates the overestimations of dust emissions during spring and winter. As discussed
 378 above, the effect of NPV on reducing dust overpredictions is more pronounced in spring than in
 379 winter, even though the NPV fractions are the highest in winter.

380 Both simulations, however, underpredict dust emissions during summer. The accuracy of
 381 simulations from the TOTAL run drops compared to those from the FPAR run, with the mean
 382 error increasing by around $0.1 \mu\text{g}/\text{m}^3$. The underpredictions in summer are likely due to the
 383 inability of the model to capture small-scale convective storms, as discussed by several previous
 384 studies (Anisimov et al., 2018; Heinold et al., 2013; Pantillon et al., 2016). Foroutan and Pleim
 385 (2017) implemented lightning assimilation and sub-grid wind distribution in the CMAQ dust
 386 model to simulate convective storms, but these modifications were not included in this study,
 387 which probably explains the systematic negative biases. The effects of NPV on dust emissions
 388 after the convective storms are included need to be further analyzed. In autumn, the
 389 implementation of NPV slightly reduces the NME by 1.3%, but increases the magnitude of NMB
 390 by 9.8% and reduces the correlation coefficient by 0.06.

391

392 **Table 2.** Seasonal statistics for simulated soil concentrations from the FPAR run and the TOTAL
 393 run. Statistics are calculated for the western states of Wyoming, Nevada, Utah, Colorado, Arizona,
 394 and New Mexico. Observations are from the IMPROVE sites. Observation and simulation values,
 395 MB, and ME are in $\mu\text{g}/\text{m}^3$, and NMB and NME are in percent.

	Spring		Summer		Autumn		Winter	
	TOTAL	FPAR	TOTAL	FPAR	TOTAL	FPAR	TOTAL	FPAR
Observation	1.03		1.00		0.76		0.44	
Simulation	1.07	1.78	0.42	0.51	0.44	0.52	0.50	0.60
MB	0.04	0.75	-0.59	-0.50	-0.32	-0.24	0.06	0.17
NMB	3.6	72.8	-58.4	-49.5	-41.5	-31.7	14.5	37.9
ME	0.59	1.01	0.62	0.57	0.52	0.51	0.43	0.48
NME	57.4	97.9	61.8	56.4	67.9	66.6	98.4	110.0
Correlation	0.52	0.44	0.41	0.42	0.25	0.31	0.29	0.27
Number of observations	1175		1142		1155		1113	

396

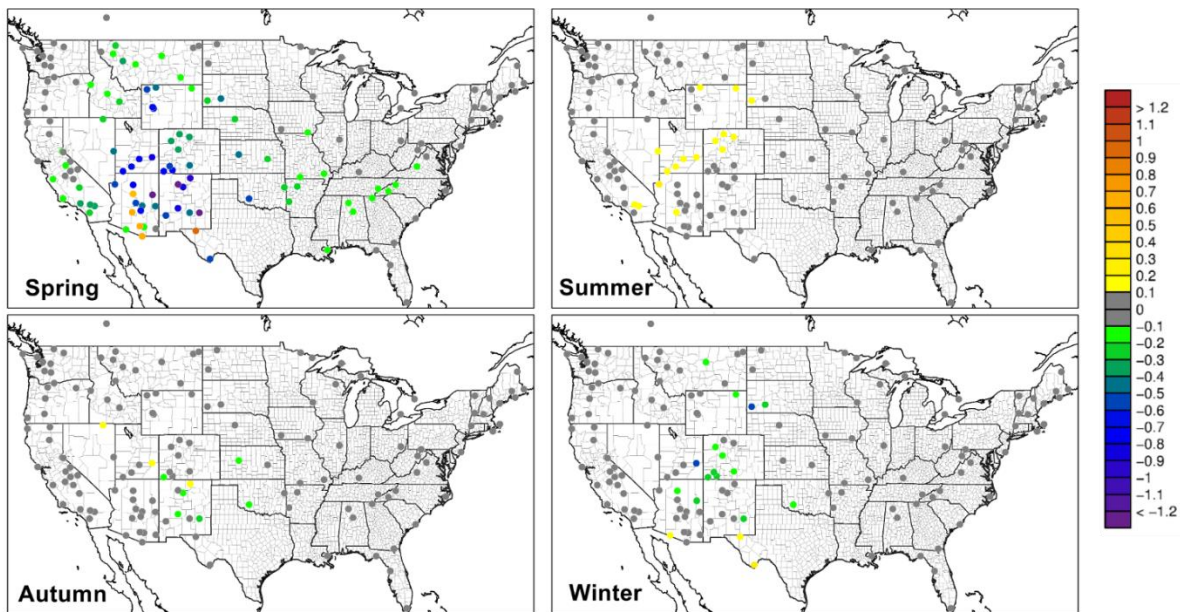
397 We further investigated the spatial distribution of differences in model biases between the
 398 two runs. The seasonal averaged changes in biases after using total vegetation data is shown in
 399 Figure 5. During spring, the averaged biases in soil concentrations are lower for the TOTAL run
 400 at 93% of all IMPROVE sites. From the statistics in Table 2, we know that these are
 401 reductions in overpredictions. The improvements are the greatest (up to $1.8 \mu\text{g}/\text{m}^3$) in northern
 402 Arizona and New Mexico, southern Utah and Colorado, and west Wyoming. Slight reductions in
 403 overpredictions are also seen in southern California, Idaho and Montana. In contrast, simulations
 404 in southern Arizona are worsen because both cases underpredicted dust emissions here
 405 throughout the year. Reasons for the underpredictions might be the inability to model sub-grid
 406 dust events or the underestimation of amount of dust transported from outside the southeastern

407 border of the U.S. The changes in biases had the similar spatial distribution in winter but are less
 408 significant.

409 During summer, slight increases in biases (by 0.1-0.3 $\mu\text{g}/\text{m}^3$) from the TOTAL run are
 410 mostly seen in northwestern Arizona, Utah, northern Colorado, and northern Wyoming. Statistics
 411 from Table 2 reveal that inclusion of NPV intensifies the underpredictions of dust emissions in
 412 these areas. Averaged soil concentrations over autumn are comparable at most of the IMPROVE
 413 sites. The difference in biases fluctuates between $\pm 0.2 \mu\text{g}/\text{m}^3$ with no apparent spatial
 414 characteristics.

415

416



417

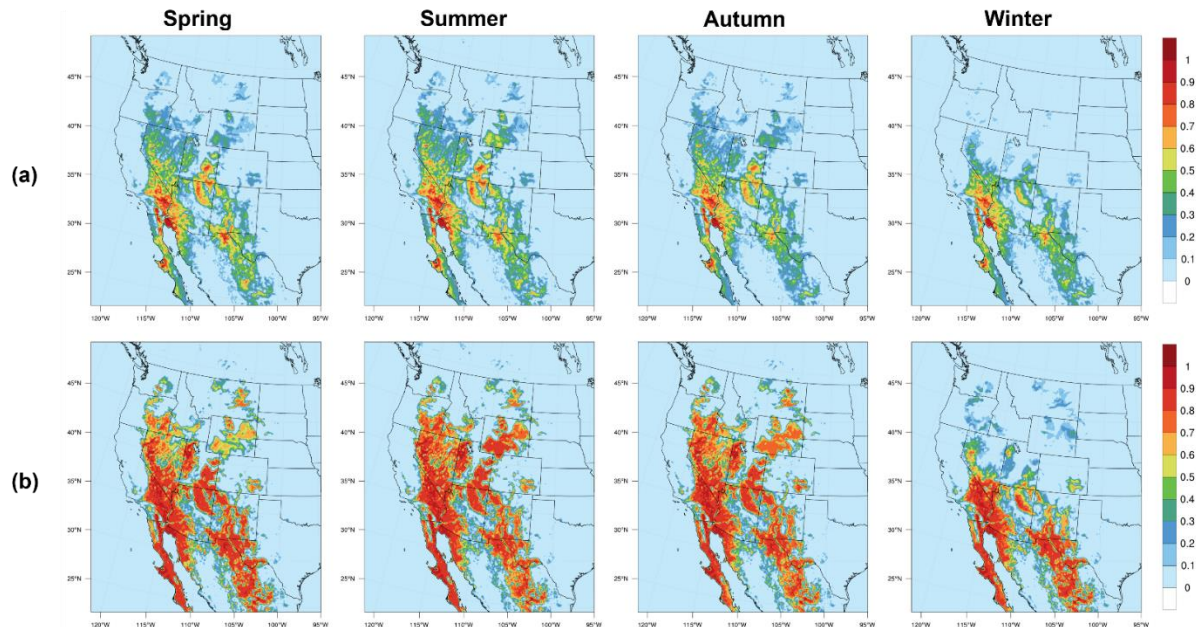
418

419 **Figure 5.** Seasonal averaged differences between the biases of soil concentrations ($\mu\text{g}/\text{m}^3$) from
 420 two runs. Observations are from the IMPROVE sites. Cold colors indicate that simulations from
 421 the TOTAL run have lower biases, thus the performance of TOTAL run is better. Warm colors
 422 indicate that the FPAR run performs better.

423 3.3. Mechanisms of Dust Emission Suppression

424 Vegetation modulates windblown dust emissions through multiple pathways. An in-depth
 425 comparison between the FPAR run and the TOTAL run simulations allows us to understand
 426 different mechanisms by which NPV impacts windblown dust emissions.

427



428 **Figure 6.** Seasonal averaged fractions of vegetation-free erodible lands from (a) the TOTAL run
 429 and (b) the FPAR run.
 430

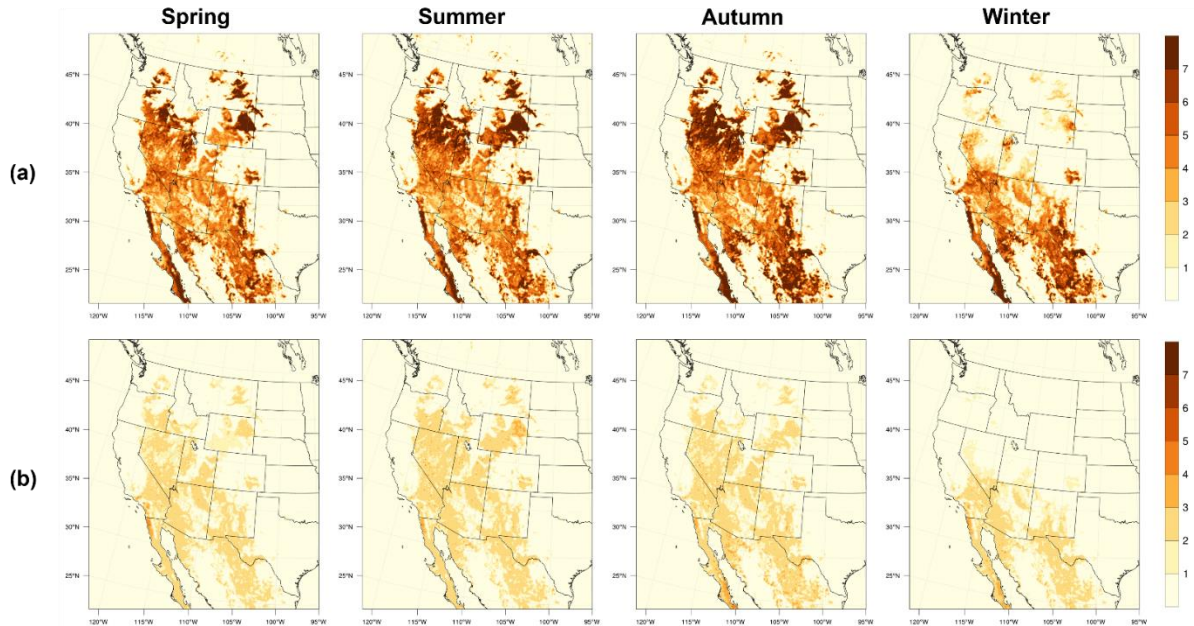
431

432 First, the vegetation coverage directly controls the fraction of land susceptible to wind
 433 erosion. In the model, the total vertical flux of dust is calculated as the weighted sum of fluxes
 434 from three erodible landuse (see Figure 1) multiplied by the fraction of land that is not covered
 435 with vegetation in each grid cell. The mechanism considered here is that vegetation covering the
 436 bare soil prevents the saltating particles from impacting the surface and smaller dust particles
 437 from being ejected to the atmosphere.

438 Figure 6 presents the fractions of vegetation-free land available for dust emissions from
 439 the two cases. The decrease in the fractions of land susceptible to dust emission is significant in
 440 all seasons after the PV is replaced with the total vegetation in the model. The reduction is the
 441 largest in autumn, followed by summer, and is comparable in spring and winter. Places with the
 442 most changes are the Salt Lake Desert, the northern Great Plain located in Nevada, Oregon, and
 443 Idaho, the northeastern Wyoming, and Montana, where the vegetation-free erodible lands
 444 decrease by over 50% in autumn. In most grid cells containing dust sources, the fractions of
 445 vegetation-free erodible lands decrease by over 0.2 in all seasons. Because the total emission of
 446 dust from each grid cell is proportional to the fractions of vegetation-free erodible land, these
 447 significant reductions suggest that one strong mechanism for NPV to reduce dust emission is to

448 prevent dust particles from leaving the surface. Nevertheless, potential underestimation of dust
 449 emissions when using total vegetation may occur due to two reasons. First, the actual fractions of
 450 land available to dust emission may be underestimated because the vegetation on non-erodible
 451 lands should not affect the exposed areas with erodible landuse. Higher resolution of landuse and
 452 vegetation inputs should help to address this issue. Second, this mechanism of dust suppression
 453 is only true for vegetation that is closer to the ground. Some NPV, such as standing dead trees,
 454 are detected by the satellite but cannot prevent soil erosion through this pathway.

455



456

457 **Figure 7.** Seasonal averages of the roughness correction factors for the threshold velocity from (a)
 458 the TOTAL run and (b) the FPAR run. Values were calculated as the averages of roughness
 459 correction factors on three erodible landuse types weighted by the fractions of each landuse.

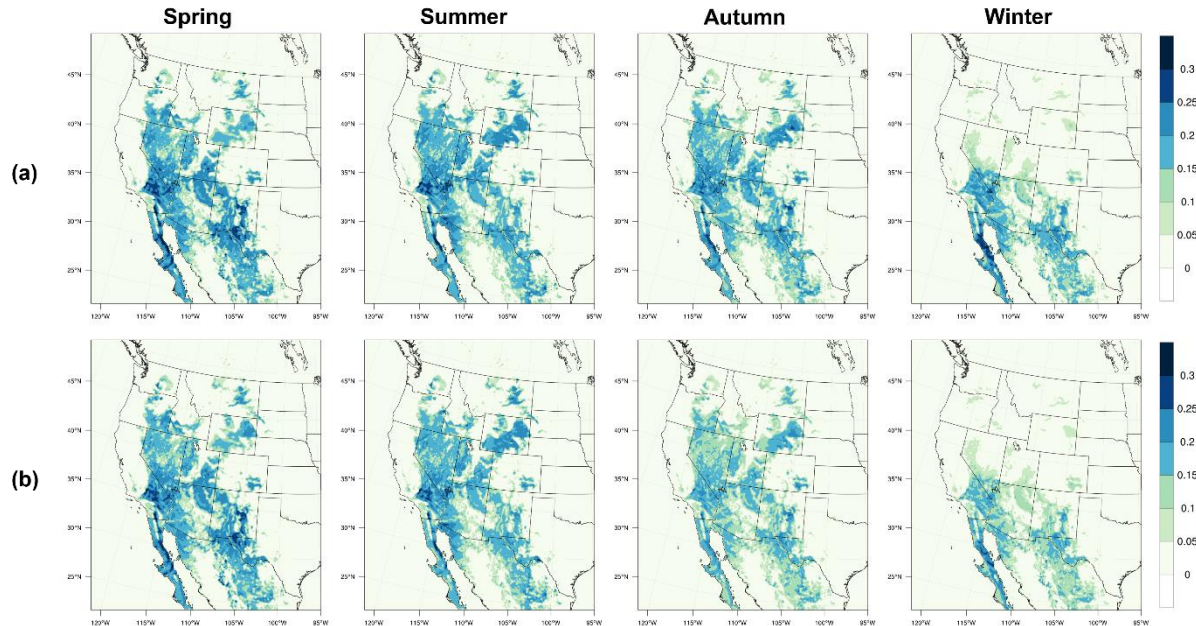
460

461 Second, the initiation of dust generation is jointly controlled by the friction velocity and
 462 its threshold value (see Eqn. 1). Emissions of windblown dust can only occur and sustain when
 463 the friction velocity exceeds the threshold velocity. Our results show that several peaks in the
 464 simulated particle concentrations in the FPAR case are absent in the TOTAL case, especially
 465 during spring. This observation suggests that NPV may prevent a number of the dust events from
 466 happening by either increasing the threshold velocity or decreasing the friction velocity, or both.
 467 Given this, we investigated the differences in modeled threshold velocity between the two
 468 simulations. Vegetation can increase the threshold velocity by extracting the wind stress exerted
 469 on the ground surface through drag partitioning process (Foroutan et al., 2017). In our model, the
 470 threshold velocity was calculated as the ideal threshold velocity modified by correction factors
 471 for soil moisture and surface roughness (see Eqn. 2). The inclusion of NPV would not change the
 472 ideal threshold velocity or soil moisture (vegetation can affect soil moisture by intercepting
 473 rainfall and uptake soil water (Teuling, 2005), but these interactions were not implemented in our

474 model), so the change in the correction factor for surface roughness can reflect the change in
 475 magnitude of threshold velocity.

476 We illustrate the seasonal averages of the correction factor for roughness calculated as
 477 the average of correction factors for three erodible landuse types weighted by the fractions of
 478 each type in Figure 7. In practice, the model actually uses the roughness correction factor
 479 separately over each landuse types, and the values shown here were not used directly in the
 480 model. However, they serve as a good representation of the magnitude of overall roughness
 481 correction factor. Seasonal averaged roughness factor is below 3 in most places across the year
 482 for the FPAR run, but significantly increases in most areas for the TOTAL run. Largest changes
 483 in roughness factor are seen in the northern Great Basin, Wyoming, Montana, western Colorado,
 484 and in the Chihuahuan Desert and the Sonoran Desert, where the averaged changes are over 4 in
 485 autumn. These NPV induced increases in roughness factor would raise the threshold velocity by
 486 over 50% in most areas and over 200% in places such as northeastern Wyoming, and hence
 487 lessen the potential for dust emissions in these regions.

488



489 **Figure 8.** Seasonal averages of the friction velocity from (a) the TOTAL run and (b) the FPAR
 490 run. Values were calculated as the averages of the friction velocities on three edible landuse
 491 types weighted by the fractions of each landuse.
 492

493

494 Third, vegetation can impact the friction velocity itself. Friction velocity is not only
 495 associated with the initiation of dust events, but also essential in determining the dust flux. The
 496 horizontal flux of dust is proportional to the third power of the friction velocity (Eq. (1)) and is
 497 thus very sensitive to its value. Vegetation elements that protrude the ground can alter the wind
 498 profile and thus change the friction velocity exerted on the surface. The effect of vegetation on

499 wind profile was accounted for using roughness length, which has a non-linear relation with
500 roughness density or fractional cover of vegetation (Eqn. (5, 6)).

501 We present the seasonal averages of the weighted mean friction velocity in Figure 8,
502 calculated using the same method as for the roughness factor. Non-linear effects of NPV on the
503 friction velocities are observed. During spring and summer, the friction velocity increases by less
504 than 0.02 m/s (below 10%) in most places, by 20-30% in the Salt Lake Desert, and decreases in
505 northeastern Wyoming and southeastern Colorado with the inclusion of NPV. In autumn and
506 winter, the increases in friction velocity due to NPV are more significant, reaching 0.03-0.05 m/s
507 (10-20%) on most erodible lands. Considering that the friction velocity increases in most of the
508 erodible lands with inclusion of NPV, which would facilitate the initiation of saltation, we can
509 conclude that the observed preventions of dust events are mainly attributed to the increases in
510 threshold velocity. However, a sensitivity analysis (Darmenova et al., 2009) showed that the
511 percentage of increase in friction velocity could lead to up to two orders of magnitude increase in
512 the dust flux when the wind velocity is low (less than 0.05 m/s), which is our case. So the
513 increases in friction velocity caused by NPV could potentially amplify the dust flux by
514 considerable amounts.

515 **4. Conclusions**

516 This paper analyzed the effects of NPV on the amount of windblown dust emissions, and
517 the underlying mechanisms on a regional scale. We implemented satellite-based total vegetation
518 data, which include both photosynthetic (PV) and non-photosynthetic vegetation (NPV), in the
519 dust module in CMAQ version 5.3 and conducted simulations for a domain covering the
520 conterminous United States for the entire year 2016. The fractional coverage of total vegetation
521 was derived from the MODIS surface reflectance data using a spectral mixture analysis (SMA)
522 method. A control run was conducted using the Moderate Resolution Imaging Spectroradiometer
523 (MODIS) Fraction of Absorbed Photosynthetically Active Radiation (FPAR) data which merely
524 presented PV fractions.

525 The PV fractions derived from the SMA approach and the MODIS FPAR have similar
526 spatial distributions across all seasons, and the difference between their averages over the
527 western U.S. are less than 2% for the entire year. The average NPV fraction over the western part
528 of the study domain is maximum from December to February and shows a minimum from June
529 to August, ranging between 26% and 40%. Higher peak in the NPV coverage compared to that of
530 the PV coverage indicates that there are sources for NPV other than senescent plant materials
531 from the same year, probably perennial dry vegetation. The NPV coverage was around 40%-50%
532 over most of the arid and semi-arid areas in the southwestern U.S. throughout the year. The areas
533 with high NPV-to-total-vegetation ratios highly overlap with the areas covered by erodible
534 landuse, suggesting that consideration of NPV was important for dust emissions from the source
535 regions.

536 Simulations of soil concentrations from both the TOTAL run and the FPAR run present
537 the seasonal variation of dust emissions and highlight locations with high dust emissions. We
538 analyzed the averaged percentage of differences in simulated soil concentrations between the two
539 simulations for all seasons. Simulated soil concentrations decrease by above 10% due to NPV in
540 most areas in southwestern U.S. from spring to autumn, and these affected areas are more

541 confined in winter. NPV induced reductions in soil concentrations are most significant in spring.
542 Regions with above 50% of reductions in soil concentrations over the entire year exclusively
543 have high NPV fractions (< 40% in winter), including parts of the Sonoran Desert, the
544 Chihuahuan Desert in New Mexico, the Great Basin in northwestern Nevada, and the Colorado
545 Plateau in southeastern Utah. Evaluation of soil concentrations against the IMPROVE
546 observations reveals that inclusion of NPV in the dust model attenuates the overpredictions at
547 93% of the sites during spring, except for those near southern Arizona. In summer, however, the
548 underpredictions in soil concentrations are accentuated, especially in Utah, Colorado, and
549 Wyoming, which potentially could be improved by implementing convective storms simulations
550 in the dust model.

551 Analyses of several parameters in the dust model to the inclusion of NPV provide
552 insights into the mechanisms by which NPV modulates dust emissions. The fraction of land
553 susceptible to wind erosion is reduced by 20% in most grid cells due to NPV, indicating that
554 NPV effectively prevents dust particles from being ejected from the ground by covering the land
555 surface. The prevention of several dust events resulted from NPV are associated with the
556 increases in threshold velocity and, in limited places, the decreases in friction velocity. On most
557 erodible lands, however, the friction velocity increases by above 10% in autumn and winter,
558 which could potentially amplify the dust flux by a few times.

559 This paper points out that dust emissions from a large portion of erodible lands are
560 modulated by the NPV. Therefore, replacing the green vegetation data currently used in many
561 dust models with the total vegetation data derived from satellite-based surface reflectance is a
562 promising approach to improve the simulations of dust emissions, and thus advance the
563 knowledge of the health impact, climate effects, and global cycling of nutrients associated with
564 windblown dust aerosols. Meanwhile, more evaluation of the calculated NPV and total
565 vegetation fractions is needed to better understand the uncertainties associated with the
566 vegetation input, which will facilitate the implementation of NPV into atmospheric dust models.

567 **Acknowledgments**

568 This work was supported by the United States Environmental Protection Agency (US
569 EPA) under the grant number 68HERC20Q0015. We thank J. P. Guerschman for assistance with
570 the vegetation data. The fractional coverage data of total vegetation is available at [https://eo-
571 data.csiro.au/remotesensing/v310/global_5km](https://eo-data.csiro.au/remotesensing/v310/global_5km). Data used in this analysis are available via the
572 Virginia Tech research repository (<https://doi.org/xxxxxxxxxxxxx>). CMAQ source code is freely
573 available via <https://github.com/usepa/cmaq.git>. Archived CMAQ versions are available from the
574 same repository. Model input data are available from the Community Modeling and Analysis
575 System (CMAS) Data Warehouse (<https://doi.org/10.15139/S3/MHNUNE>). The authors declare
576 that there is no conflict of interest related to this work.

577 **References**

578 Al-Hemoud, A., Al-Dousari, A., Misak, R., Al-Sudairawi, M., Naseeb, A., Al-Dashti, H., & Al-
579 Dousari, N. (2019). Economic Impact and Risk Assessment of Sand and Dust Storms (SDS)
580 on the Oil and Gas Industry in Kuwait. *Sustainability*, *11*(1). doi:10.3390/su11010200

- 581 Anisimov, A., Axisa, D., Kucera, P. A., Mostamandi, S., & Stenchikov, G. (2018). Observations
582 and Cloud-Resolving Modeling of Haboob Dust Storms Over the Arabian Peninsula.
583 *Journal of Geophysical Research: Atmospheres*, 123(21), 12147-12179.
584 doi:10.1029/2018JD028486
- 585 Appel, K. W., Bash, J. O., Fahey, K. M., Foley, K. M., Gilliam, R. C., Hogrefe, C., . . . Wong, D.
586 C. (2020). The Community Multiscale Air Quality (CMAQ) Model Versions 5.3 and 5.3.1:
587 System Updates and Evaluation. *Geosci. Model Dev. Discuss.*, 2020, 1-41.
588 doi:10.5194/gmd-2020-345
- 589 Asner, G. P., & Heidebrecht, K. B. (2002). Spectral unmixing of vegetation, soil and dry carbon
590 cover in arid regions: Comparing multispectral and hyperspectral observations.
591 *International Journal of Remote Sensing*, 23(19), 3939-3958.
592 doi:10.1080/01431160110115960
- 593 Baddock, M. C., Strong, C. L., Leys, J. F., Heidenreich, S. K., Tews, E. K., & McTainsh, G. H.
594 (2014). A visibility and total suspended dust relationship. *Atmospheric Environment*, 89,
595 329-336. doi:https://doi.org/10.1016/j.atmosenv.2014.02.038
- 596 Cao, X., Chen, J., Matsushita, B., & Imura, H. (2010). Developing a MODIS-based index to
597 discriminate dead fuel from photosynthetic vegetation and soil background in the Asian
598 steppe area. *International Journal of Remote Sensing*, 31(6), 1589-1604.
599 doi:10.1080/01431160903475274
- 600 Csavina, J., Field, J., Taylor, M. P., Gao, S., Landazuri, A., Betterton, E. A., & Saez, A. E. (2012).
601 A review on the importance of metals and metalloids in atmospheric dust and aerosol from
602 mining operations. *Sci Total Environ*, 433, 58-73. doi:10.1016/j.scitotenv.2012.06.013
- 603 Darmenova, K., Sokolik, I. N., Shao, Y., Marticorena, B., & Bergametti, G. (2009). Development
604 of a physically based dust emission module within the Weather Research and Forecasting
605 (WRF) model: Assessment of dust emission parameterizations and input parameters for
606 source regions in Central and East Asia. *Journal of Geophysical Research*, 114(D14).
607 doi:10.1029/2008jd011236
- 608 Duncan Fairlie, T., Jacob, D. J., & Park, R. J. (2007). The impact of transpacific transport of
609 mineral dust in the United States. *Atmospheric Environment*, 41(6), 1251-1266.
610 doi:10.1016/j.atmosenv.2006.09.048
- 611 F. FeÂcan, B. M. a. G. B. (1999). Parametrization of the increase of the aeolian erosion threshold
612 wind friction velocity due to soil moisture for arid and semi-arid areas. *Annales*
613 *Geophysicae*.
- 614 Foroutan, H., & Pleim, J. E. (2017). Improving the simulation of convective dust storms in
615 regional-to-global models. *J Adv Model Earth Syst*, 9(5), 2046-2060.
616 doi:10.1002/2017MS000953

- 617 Foroutan, H., Young, J., Napelenok, S., Ran, L., Appel, K. W., Gilliam, R. C., & Pleim, J. E. (2017).
618 Development and evaluation of a physics-based windblown dust emission scheme
619 implemented in the CMAQ modeling system. *J Adv Model Earth Syst*, 9(1), 585-608.
620 doi:10.1002/2016MS000823
- 621 Guerschman, Hill, M. J., Renzullo, L. J., Barrett, D. J., Marks, A. S., & Botha, E. J. (2009).
622 Estimating fractional cover of photosynthetic vegetation, non-photosynthetic vegetation
623 and bare soil in the Australian tropical savanna region upscaling the EO-1 Hyperion and
624 MODIS sensors. *Remote Sensing of Environment*, 113(5), 928-945.
625 doi:10.1016/j.rse.2009.01.006
- 626 Guerschman, Scarth, P. F., McVicar, T. R., Renzullo, L. J., Malthus, T. J., Stewart, J. B., . . .
627 Trevithick, R. (2015). Assessing the effects of site heterogeneity and soil properties when
628 unmixing photosynthetic vegetation, non-photosynthetic vegetation and bare soil fractions
629 from Landsat and MODIS data. *Remote Sensing of Environment*, 161, 12-26.
630 doi:10.1016/j.rse.2015.01.021
- 631 Hagen, L. J. (1996). Crop Residue Effects On Aerodynamic Processes and Wind Erosion.
632 *Theoretical and Applied Climatology*.
- 633 Heinold, B., Knippertz, P., Marsham, J. H., Fiedler, S., Dixon, N. S., Schepanski, K., . . . Tegen, I.
634 (2013). The role of deep convection and nocturnal low-level jets for dust emission in
635 summertime West Africa: Estimates from convection-permitting simulations. *J Geophys*
636 *Res Atmos*, 118(10), 4385-4400. doi:10.1002/jgrd.50402
- 637 Ji, C., Li, X., Wei, H., & Li, S. (2020). Comparison of Different Multispectral Sensors for
638 Photosynthetic and Non-Photosynthetic Vegetation-Fraction Retrieval. *Remote Sensing*,
639 12(1). doi:10.3390/rs12010115
- 640 Kang, J.-Y., Tanaka, T. Y., & Mikami, M. (2014). Effect of dead leaves on early spring dust
641 emission in East Asia. *Atmospheric Environment*, 86, 35-46.
642 doi:10.1016/j.atmosenv.2013.12.007
- 643 Kellogg, C. A., & Griffin, D. W. (2006). Aerobiology and the global transport of desert dust. *Trends*
644 *Ecol Evol*, 21(11), 638-644. doi:10.1016/j.tree.2006.07.004
- 645 Klose, M., Jorba, O., Gonçalves Ageitos, M., Escribano, J., Dawson, M. L., Obiso, V., . . . Pérez
646 García-Pando, C. (2021). Mineral dust cycle in the Multiscale Online Nonhydrostatic
647 Atmosphere Chemistry model (MONARCH) Version 2.0. *Geosci. Model Dev. Discuss.*
648 doi:10.5194/gmd-2021-32
- 649 Knippertz, P. (2017). Mineral Dust Generation across Northern Africa and Its Impacts. In *Oxford*
650 *Research Encyclopedia of Climate Science*.
- 651 Kurosaki, Y., Shinoda, M., Mikami, M., & Nandintsetseg, B. (2011). Effects of Soil and Land
652 Surface Conditions in Summer on Dust Outbreaks in the Following Spring in a Mongolian

- 653 Grassland. *SOLA*, 7, 69-72. doi:10.2151/sola.2011-018
- 654 LeGrand, S. L., Polashenski, C., Letcher, T. W., Creighton, G. A., Peckham, S. E., & Cetola, J. D.
655 (2019). The AFWA dust emission scheme for the GOCART aerosol model in WRF-Chem
656 v3.8.1. *Geoscientific Model Development*, 12(1), 131-166. doi:10.5194/gmd-12-131-2019
- 657 Li, X., Zheng, G., Wang, J., Ji, C., Sun, B., & Gao, Z. (2016). Comparison of Methods for
658 Estimating Fractional Cover of Photosynthetic and Non-Photosynthetic Vegetation in the
659 Otindag Sandy Land Using GF-1 Wide-Field View Data. *Remote Sensing*, 8(10).
660 doi:10.3390/rs8100800
- 661 Li, Z., & Guo, X. (2015). Remote sensing of terrestrial non-photosynthetic vegetation using
662 hyperspectral, multispectral, SAR, and LiDAR data. *Progress in Physical Geography:
663 Earth and Environment*, 40(2), 276-304. doi:10.1177/0309133315582005
- 664 Lin, X., Niu, J., Yu, X., Berndtsson, R., Wu, S., & Xie, S. (2021). Maize residue effects on PM2.5,
665 PM10, and dust emission from agricultural land. *Soil and Tillage Research*, 205.
666 doi:10.1016/j.still.2020.104738
- 667 Lu, H., & Shao, Y. (1999). A new model for dust emission by saltation bombardment. *Journal of
668 Geophysical Research: Atmospheres*, 104(D14), 16827-16842. doi:10.1029/1999jd900169
- 669 Malm, W. C. (1994). Spatial and seasonal trends in particle concentration and optical extinction in
670 the United States. *Journal of Geophysical Research*, VOL. 99, NO. D1, PAGES 1347-137.
- 671 Marsett, R. C., Qi, J., Heilman, P., Biedenbender, S. H., Carolyn Watson, M., Amer, S., . . . Marsett,
672 R. (2006). Remote Sensing for Grassland Management in the Arid Southwest. *Rangeland
673 Ecology & Management*, 59(5), 530-540. doi:10.2111/05-201r.1
- 674 Mougin, E., Lo Seen, D., Ramba, S., Gaston, A., & Hiernaux, P. (1995). A Regional Sahelian
675 Grassland Model To Be Coupled with Multispectral Satellite Data. I: Model Description
676 and Validation.
- 677 Nakao, M., Ishihara, Y., Kim, C. H., & Hyun, I. G. (2018). The Impact of Air Pollution, Including
678 Asian Sand Dust, on Respiratory Symptoms and Health-related Quality of Life in
679 Outpatients With Chronic Respiratory Disease in Korea: A Panel Study. *J Prev Med Public
680 Health*, 51(3), 130-139. doi:10.3961/jpmph.18.021
- 681 Nandintsetseg, B., & Shinoda, M. (2015). Land surface memory effects on dust emission in a
682 Mongolian temperate grassland. *Journal of Geophysical Research-Biogeosciences*, 120(3),
683 414-427. doi:10.1002/2014jg002708
- 684 Okin, G. S., Clarke, K. D., & Lewis, M. M. (2013). Comparison of methods for estimation of
685 absolute vegetation and soil fractional cover using MODIS normalized BRDF-adjusted
686 reflectance data. *Remote Sensing of Environment*, 130, 266-279.
687 doi:10.1016/j.rse.2012.11.021

- 688 Pantillon, F., Knippertz, P., Marsham, J. H., Panitz, H.-J., & Bischoff-Gauss, I. (2016). Modeling
689 haboob dust storms in large-scale weather and climate models. *Journal of Geophysical*
690 *Research: Atmospheres*, *121*(5), 2090-2109. doi:10.1002/2015jd024349
- 691 Pierre, C., Kergoat, L., Bergametti, G., Mougin, É., Baron, C., Abdourhamane Toure, A., . . . Delon,
692 C. (2015). Modeling vegetation and wind erosion from a millet field and from a rangeland:
693 Two Sahelian case studies. *Aeolian Research*, *19*, 97-111.
694 doi:10.1016/j.aeolia.2015.09.009
- 695 Qi, J., & Wallace, O. (2002). Biophysical Attributes Estimation from Satellite Images in Arid
696 Regions.
- 697 R. L. Miller, I. T. (1998). Climate Response to Soil Dust Aerosols. *Journal of Climate*.
- 698 Ran, L., Pleim, J., Gilliam, R., Binkowski, F. S., Hogrefe, C., & Band, L. (2016). Improved
699 meteorology from an updated WRF/CMAQ modeling system with MODIS vegetation and
700 albedo. *Journal of Geophysical Research: Atmospheres*, *121*(5), 2393-2415.
701 doi:10.1002/2015jd024406
- 702 Raupach, M. R., Gillette, D. A., & Leys, J. F. (1993). The effect of roughness elements on wind
703 erosion threshold. *Journal of Geophysical Research: Atmospheres*, *98*(D2), 3023-3029.
704 doi:<https://doi.org/10.1029/92JD01922>
- 705 Scarth, P. F., Röder, A., & Schmidt, M. (2011). *Tracking Grazing Pressure and Climate Interaction*
706 *- The Role of LANDSAT Fractional Cover in Time Series Analysis*. Paper presented at the
707 Proceedings of the 15th Australasian Remote Sensing and Photogrammetry Conference,
708 Australia: Alice Springs.
- 709 Seager, R., Feldman, J., Lis, N., Ting, M., Williams, A. P., Nakamura, J., . . . Henderson, N. (2018).
710 Whither the 100th Meridian? The Once and Future Physical and Human Geography of
711 America's Arid-Humid Divide. Part II: The Meridian Moves East. *Earth Interactions*,
712 *22*(5), 1-24. doi:10.1175/ei-d-17-0012.1
- 713 Seager, R., Lis, N., Feldman, J., Ting, M., Williams, A. P., Nakamura, J., . . . Henderson, N. (2018).
714 Whither the 100th Meridian? The Once and Future Physical and Human Geography of
715 America's Arid-Humid Divide. Part I: The Story So Far. *Earth Interactions*, *22*(5), 1-22.
716 doi:10.1175/ei-d-17-0011.1
- 717 Shao, Y. P., Raupach, M. R., & Leys, J. F. (1996). A model for predicting aeolian sand drift and
718 dust entrainment on scales from paddock to region. *Soil Research*, *34*(3), 309-342.
719 Retrieved from <https://doi.org/10.1071/SR9960309>
- 720 Shinoda, M., Gillies, J. A., Mikami, M., & Shao, Y. (2011). Temperate grasslands as a dust source:
721 Knowledge, uncertainties, and challenges. *Aeolian Research*, *3*(3), 271-293.
722 doi:10.1016/j.aeolia.2011.07.001

- 723 Tegen, I., Harrison, S. P., Kohfeld, K., Prentice, I. C., Coe, M., & Heimann, M. (2002). Impact of
724 vegetation and preferential source areas on global dust aerosol: Results from a model study.
725 *Journal of Geophysical Research: Atmospheres*, *107*(D21), AAC 14-11-AAC 14-27.
726 doi:10.1029/2001jd000963
- 727 Teuling, A. J. (2005). Improved understanding of soil moisture variability dynamics. *Geophysical*
728 *Research Letters*, *32*(5). doi:10.1029/2004gl021935
- 729 Xi, X., & Sokolik, I. N. (2015). Seasonal dynamics of threshold friction velocity and dust emission
730 in Central Asia. *Journal of Geophysical Research: Atmospheres*, *120*(4), 1536-1564.
731 doi:10.1002/2014jd022471
- 732 Zhang, K., O'Donnell, D., Kazil, J., Stier, P., Kinne, S., Lohmann, U., . . . Feichter, J. (2012). The
733 global aerosol-climate model ECHAM-HAM, version 2: sensitivity to improvements in
734 process representations. *Atmospheric Chemistry and Physics*, *12*(19), 8911-8949.
735 doi:10.5194/acp-12-8911-2012